

Supplemental Information

Functional Network Organization of the Human Brain

Jonathan D. Power, Alexander L. Cohen, Steven M. Nelson, Gagan S. Wig, Kelly Anne Barnes, Jessica A. Church, Alecia C. Vogel, Timothy O. Laumann, Fran M. Miezin, Bradley L. Schlaggar, and Steven E. Petersen

Supplemental Data:

Meta-analysis	# Studies	# Subjects	# ROIs	
Button-pushing	12	310	46	
Verb Generation	9	220	47	
Reading	5	116	60	
Sustained Task-Induced Deactivations	11	217	9	
Transient Task-Induced Deactivations	11	217	8	
Sustained Task Block Activations	11	217	17	
On-Cue Task Block Activations	11	217	47	
Error Commission	8	176	48	
Memory Retrieval	5	128	40	
Total meta-analytic ROIs			322	
meta-analytic ROI set (overlaps removed)			151	
Total fc-Mapping ROIs			254	
fc-Mapping ROI set (overlaps removed)			193	
Combined ROI set (overlaps removed)			264	
	# Subjects (M/F)	Age (s.d.)	RMS (s.d.)	# Frames (s.d)
Cohort 1	52 (21/31)	25.2 (2.5)	0.17 (0.07)	348 (77)
Cohort 2	53 (22/31)	25.3 (2.4)	0.19 (0.08)	362 (85)

Table S1: ROI derivation and cohort attributes. At top, the fMRI meta-analyses, studies included, subjects included, and number of ROIs identified from each meta-analysis. 322 individual ROIs were identified, which were consolidated to 151 final meta-analytic ROIs by spatial averaging. fc-Mapping identified 254 ROIs, and a representative set of 193 non-overlapping ROIs is presented in this report. The combined ROI set merged the meta-analytic set and the fc-Mapping set for a total of 264 ROIs. Two matched cohorts of healthy young adults provided the data for network analysis. Number of subjects, ages (in years), movement estimates (RMS movement in mm), and number of time points in the scans are shown for each cohort.

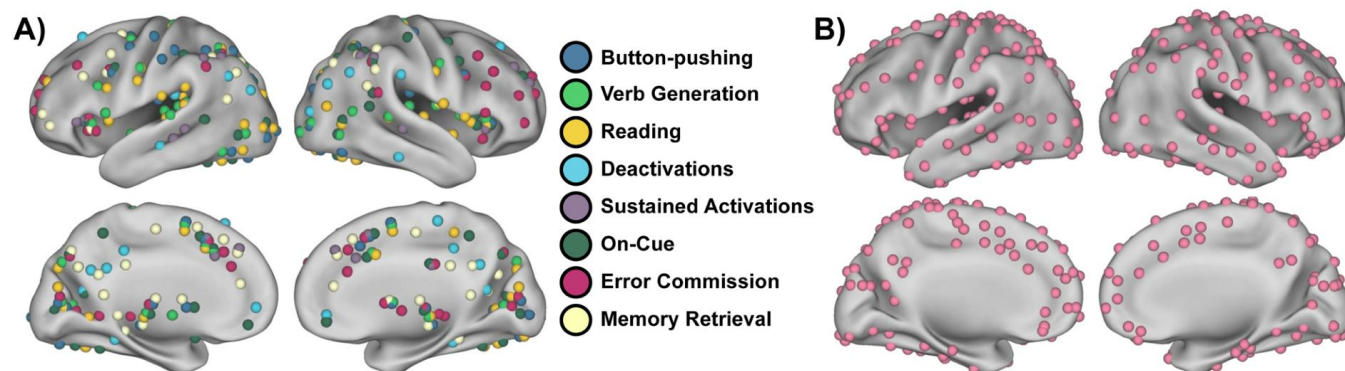


Figure S1: Putative functional areas. (A) The 322 putative functional areas identified from the meta-analytic approach. ROIs in subcortical nuclei are pulled to the medial surface, and cerebellar ROIs are not shown. (B) The 254 putative functional areas identified using fc-Mapping techniques. This method only identifies cortical ROIs. ROIs are shown pasted to an inflated PALS surface (Van Essen, 2001; Van Essen, 2005).

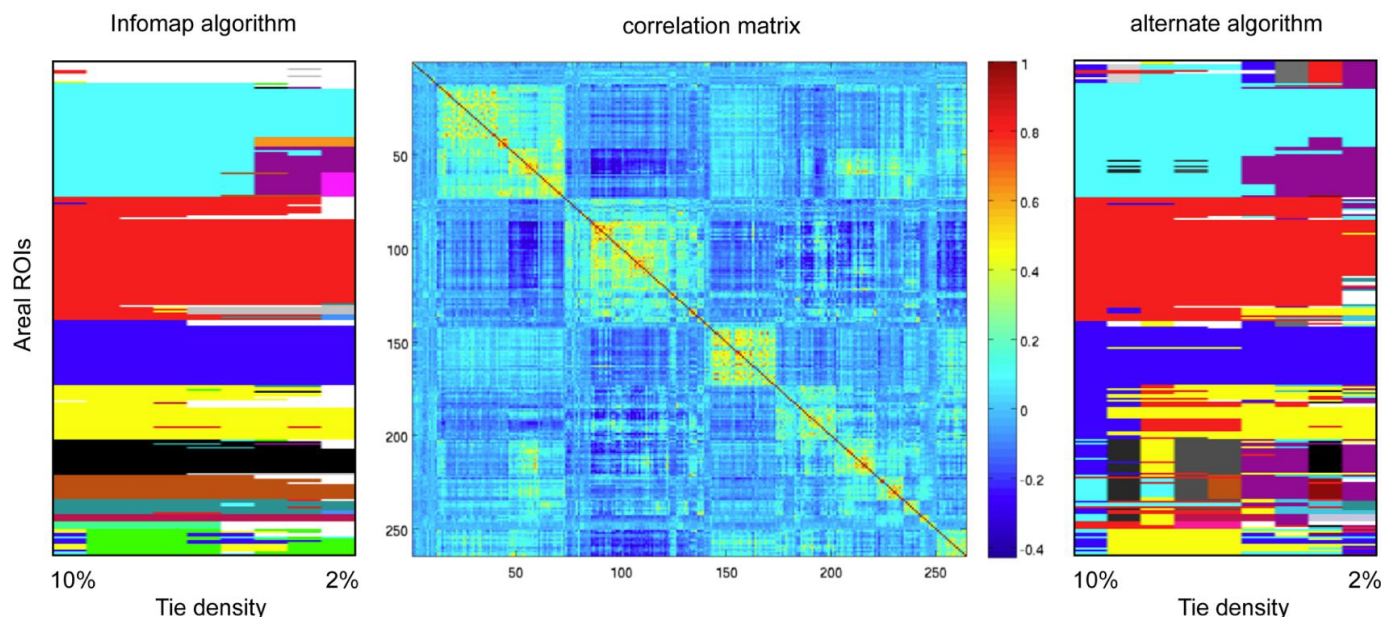


Figure S2: Infomap and an alternate subgraph detection algorithm operating upon the same network. At left, the assignments of areal nodes into subgraphs by the Infomap algorithm, one of the best-performing subgraph detection algorithms presently available (Rosvall & Bergstrom, 2008; Fortunato, 2010). Middle, the correlation matrix that defines the areal network in the main cohort. Right, the assignment of nodes into subgraphs by an alternate community detection algorithm that optimizes Newman's modularity using spectral partitioning (Newman, 2006). Subgraphs with the Infomap algorithm are clearly more stable across thresholds, and the sensitivity to small subgraphs is also higher using the Infomap algorithm (the basis for the black, brown, teal and magenta subgraphs at left can be seen in the correlation matrix; these subgraphs are only reliably separated by Infomap). All subgraphs with fewer than 4 nodes are colored white.

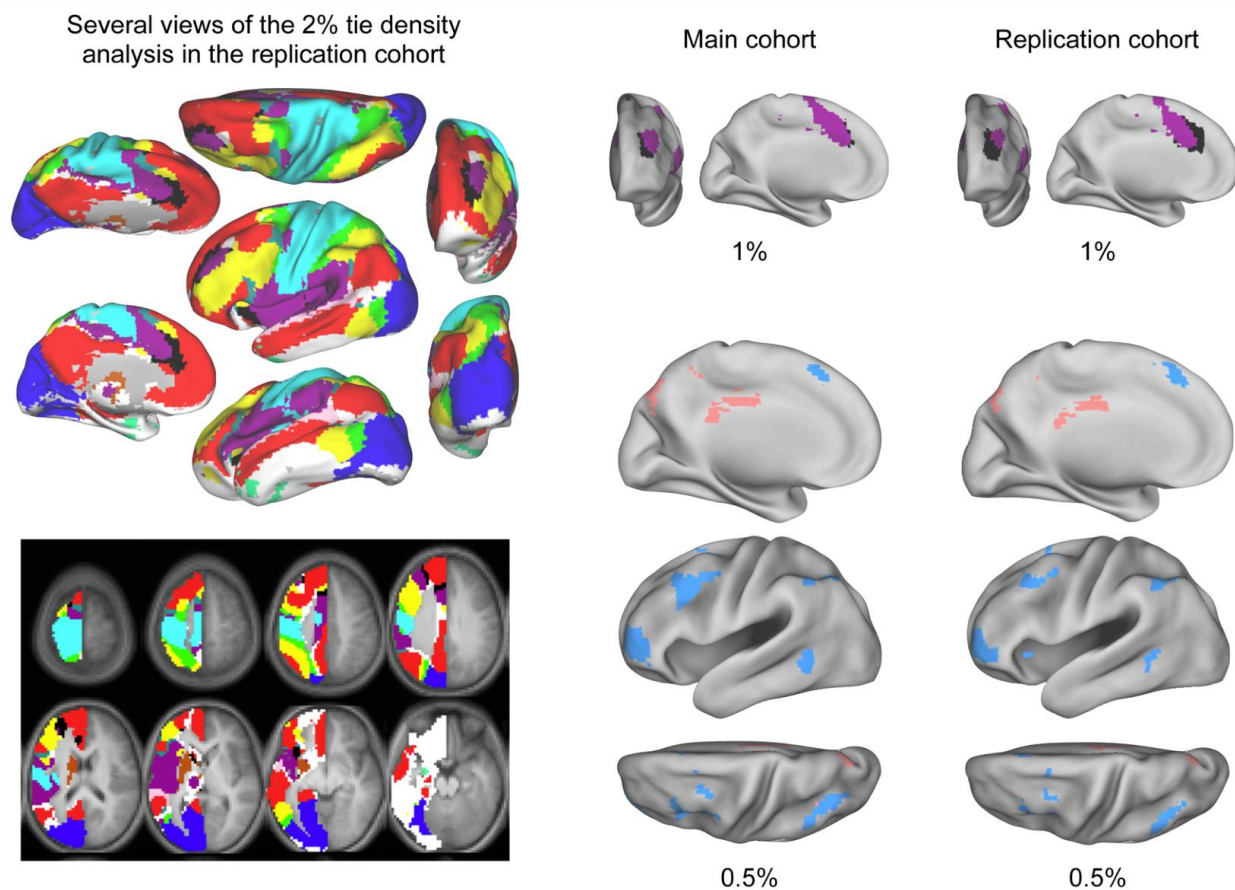


Figure S3: Additional views of the modified voxelwise analysis and additional instances of replicating subgraphs. To contextualize the data presented in the main figures, modified voxelwise subgraphs are presented in surface and slice format for the 2%tie density analysis in the replication cohort. For the black, light blue, and salmon (gray) subgraphs addressed in Figure 4, replication analyses are shown here. Data are taken from 1% analysis (the same used in Figure 3) and from the 0.5% analysis (the same used in Figure 4).

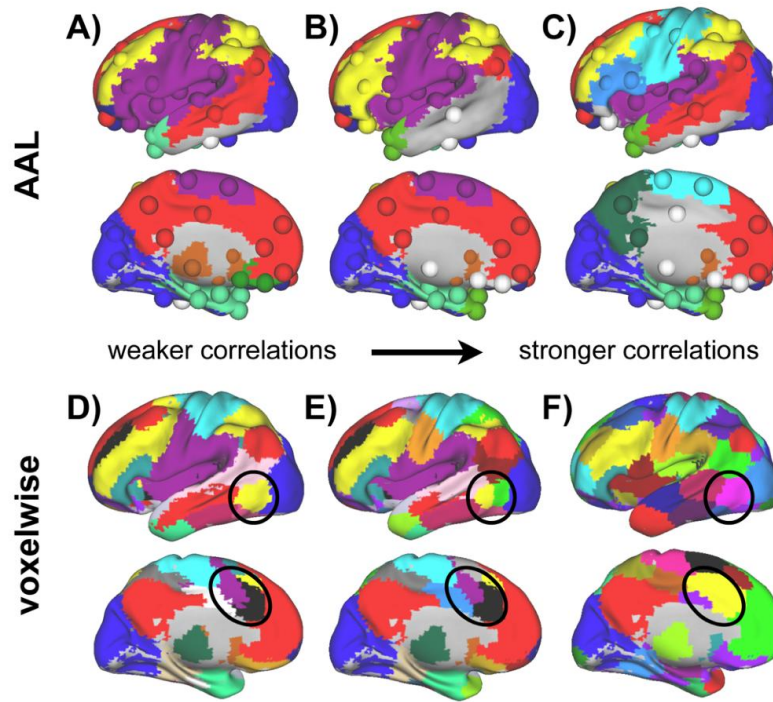


Figure S4: Subgraphs in AAL-based and voxel-based graphs have difficulty representing major functional systems. (A-C) Subgraph assignments in the AAL-based graph are shown for analyses performed at (A) 9%, (B) 7%, and (C) 5% tie density in the replication cohort (the network becomes severely fragmented below 5% tie density). Assignments across cohorts are nearly identical ($NMI = 0.96 \pm 0.04$ over thresholds). Corresponding thresholds were $r > 0.26$, $r > 0.33$, and $r > 0.39$. Spheres indicate the center of mass of the parcel, and surface colors indicate the extent of the parcel. All subgraphs with fewer than 3 members are colored white (with base gray surface). Several distributed functional systems such as dorsal attention or ventral attention systems are not represented at all, and even the default mode system is poorly represented. (D-F) Subgraph assignments in networks formed using all voxels within the AAL atlas ($N = 40,100$) are shown in the bottom row for analyses at (D) 5%, (E) 3%, and (F) 1% tie density in the replication cohort. Corresponding thresholds were $r > 0.18$, $r > 0.23$, and $r > 0.33$. All subgraphs with fewer than 250 voxels are colored white. At higher thresholds local correlations come to dominate network organization, leading to a patchwork subgraph structure across the cortex (see the circled regions in lateral temporal and medial prefrontal cortex). In (F), 56 subgraphs are present, and patches with identical colors may not actually be in the same subgraph (this is the only Figure in which colors do not indicate unique subgraph assignments; it is impossible to find 56 visually discriminable colors). Colors within circled areas (yellow and pink) represent single subgraphs.

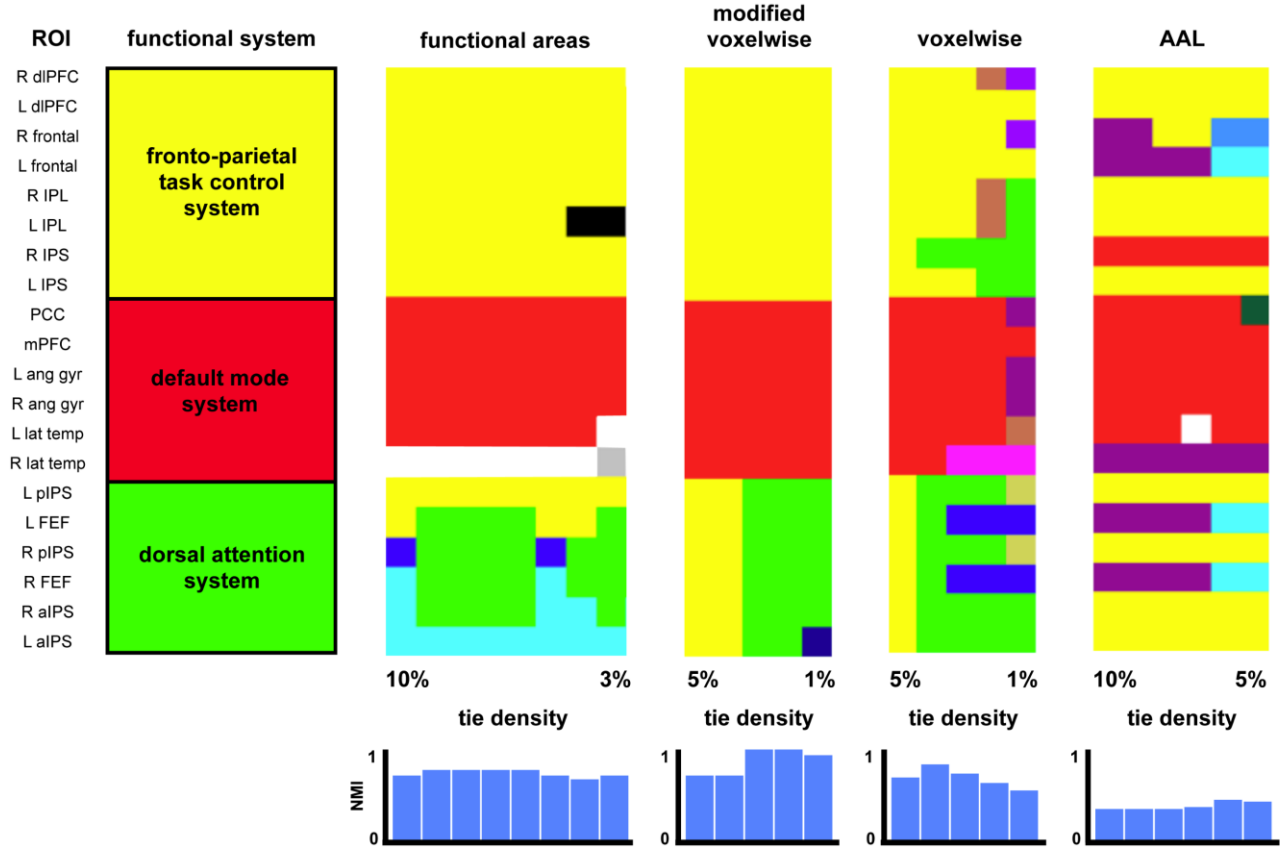


Figure S5: Correspondence between functional systems and subgraphs in each network. At right, task-defined regions of interest (ROIs) from three major functional systems are shown. In the next four columns, the subgraph assignment of the node nearest to each region (determined by Euclidean distance between centers of mass) is indicated by color over a range of thresholds for each network examined in this report. The areal and modified voxelwise graphs have visibly higher and stabler correspondence of subgraph structure to functional systems than the voxelwise or AAL-based networks. The bar plots under the charts quantify this correspondence with normalized mutual information. For the four respective networks, NMI are 0.72 ± 0.06 , 0.85 ± 0.15 , 0.72 ± 0.11 , and 0.37 ± 0.04 . A one-factor (group) ANOVA shows a significant effect of group ($p < 10^{-6}$). The AAL-based graph has a significantly lower NMI than all other groups (all $p < 0.001$ by two-sample two-tail t-tests). Note that NMI increases with threshold in the modified voxelwise graph but decreases with threshold in the standard voxelwise graph. Regions adapted from (Dosenbach, 2006; Dosenbach, 2007), p.c. Marc Raichle, and MNI coordinates for these ROIs are found in Table S3.

Source	System	Name	X	Y	Z
Dosenbach et al, 2007	Fronto-parietal task control	R dIPFC	46	28	31
Dosenbach et al, 2007	Fronto-parietal task control	L dIPFC	-44	27	33
Dosenbach et al, 2007	Fronto-parietal task control	R frontal	44	8	34
Dosenbach et al, 2007	Fronto-parietal task control	L frontal	-42	7	36
Dosenbach et al, 2007	Fronto-parietal task control	R IPL	54	-44	43
Dosenbach et al, 2007	Fronto-parietal task control	L IPL	-53	-50	39
Dosenbach et al, 2007	Fronto-parietal task control	R IPS	32	-59	41
Dosenbach et al, 2007	Fronto-parietal task control	L IPS	-32	-58	46
p.c. Marc Raichle	Default mode network	PCC	1	-51	29
p.c. Marc Raichle	Default mode network	mPFC	-1	61	22
p.c. Marc Raichle	Default mode network	L AG	-48	-66	34
p.c. Marc Raichle	Default mode network	R AG	53	-61	35
p.c. Marc Raichle	Default mode network	L lat temp	-65	-23	-9
p.c. Marc Raichle	Default mode network	R lat temp	61	-21	-12
p.c. Marc Raichle	Dorsal attention	L pIPS	-26	-65	52
p.c. Marc Raichle	Dorsal attention	L FEF	-29	-5	55
p.c. Marc Raichle	Dorsal attention	R pIPS	28	-65	51
p.c. Marc Raichle	Dorsal attention	R FEF	31	-5	54
p.c. Marc Raichle	Dorsal attention	R aIPS	43	-36	46
p.c. Marc Raichle	Dorsal attention	L aIPS	-45	-37	48

Table S3, related to Figure S5 and Figure 3: The source, functional system, name, and locations (in MNI space) of the regions of interest used in Figure S5.

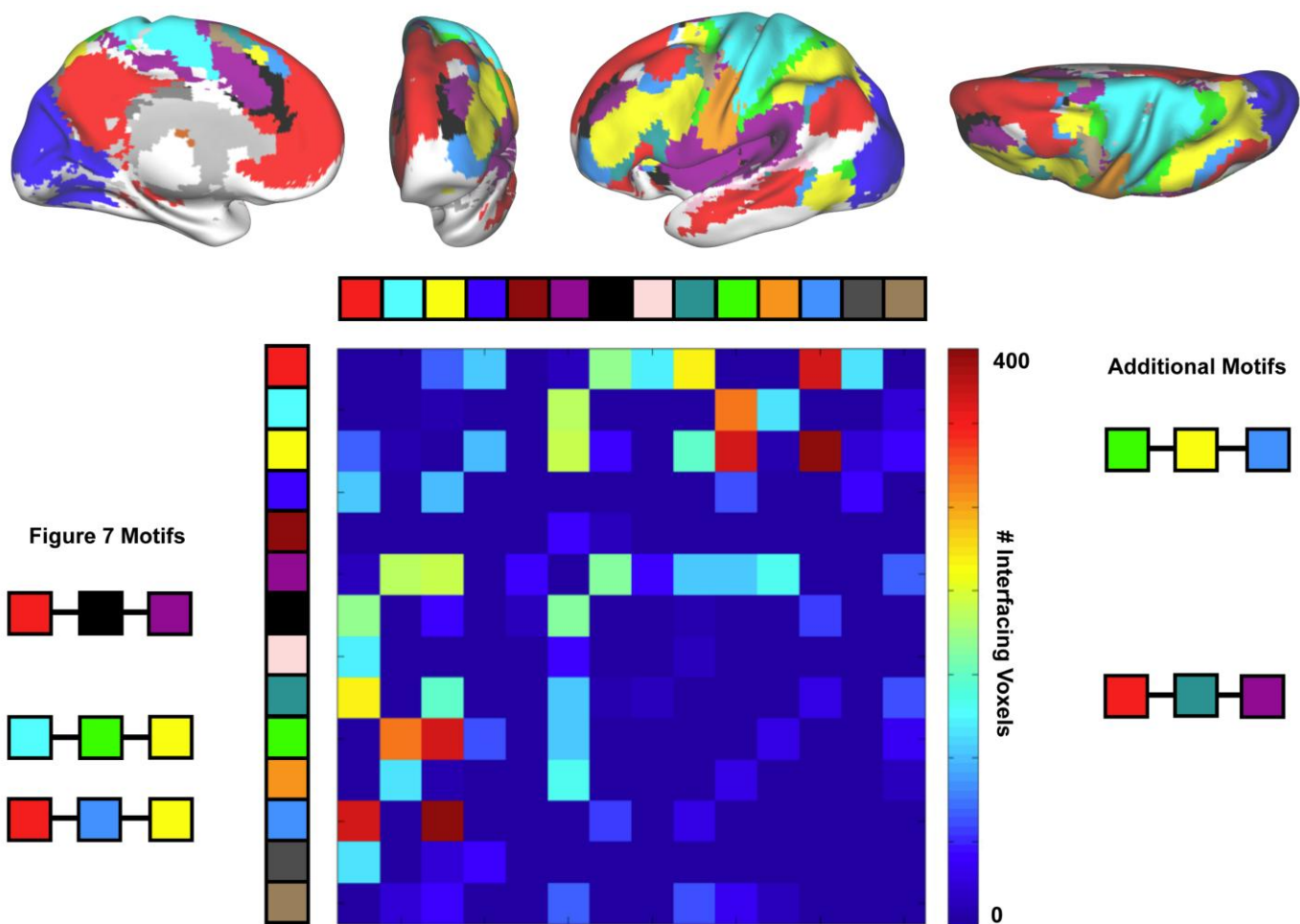


Figure S6: Detection of motifs. Subgraphs for the 1% tie density modified voxelwise analysis in the replication cohort are displayed on a brain surface. The chart plots the number of interfacing voxels between subgraphs, corresponding to data shown in Figure 7. Three-step interposed motifs are visible to the eye on the brain surface (e.g., yellow, light blue, red). Examination of the light blue row (row 12) reveals that 88% of light blue interfaces are with yellow or red, whereas red is only 2.6% of yellow's interface and yellow is only 2.6% of red's interface. Other instances of this 3-step motif are displayed to the left and right of the chart. These and other motifs are present at other thresholds.

Supplemental Experimental Procedures:

Subjects

Healthy young adults were recruited from the Washington University campus and the surrounding community. All subjects were native English speakers and right-handed. All subjects gave informed consent and were compensated for their participation.

Datasets and Data Collection

This study utilized multiple datasets. The first and second datasets were used for meta-analytic and fc-Mapping analyses, respectively. The third dataset was used for rs-fcMRI network analysis.

The first ($N > 300$, detailed in Table S1) and second datasets ($N=40$) were acquired on a Siemens 1.5 Tesla MAGNETOM Vision MRI scanner (Erlangen, Germany), as described in (Dosenbach et al., 2010). Structural images were obtained using a sagittal magnetization-prepared rapid gradient echo (MP-RAGE) three-dimensional T1-weighted sequence ($TE = 4$ ms, $TR = 9.7$ ms, $TI = 300$ ms, flip angle = 12° , 128 slices with $1.25 \times 1 \times 1$ mm voxels). Functional images were obtained using an asymmetric spin echo echo-planar sequence sensitive to blood oxygen level- dependent (BOLD) contrast ($T2^*$ evolution time = 50 ms, flip angle = 90° , in-plane resolution 3.75×3.75 mm; volume $TR = 2.5$ s). Magnetization steady state was assumed after 10 seconds. Whole brain coverage for the functional data was obtained using 16 contiguous interleaved 8 mm axial slices, acquired parallel to the plane transecting the anterior and posterior commissure (AC-PC plane).

The third dataset ($N=106$: a 53 subject cohort, 52 subject cohort, and an additional single subject) was acquired on a Siemens MAGNETOM Tim Trio 3.0T Scanner with a Siemens 12 channel Head Matrix Coil (Erlangen, Germany). A T1-weighted sagittal MP-RAGE structural image was obtained ($TE = 3.06$ ms, TR -partition = 2.4 s, $TI = 1000$ ms, flip angle = 8° , 176 slices with $1 \times 1 \times 1$ mm voxels). A T2-weighted turbo spin echo structural image ($TE = 84$ ms, $TR = 6.8$ s, 32 slices with $2 \times 1 \times 4$ mm voxels) in the same anatomical plane as the BOLD images was also obtained to improve alignment to an atlas. Functional images were obtained using a BOLD contrast sensitive gradient echo echo-planar sequence ($TE = 27$ ms, flip angle = 90° , in-plane resolution = 4×4 mm; volume $TR = 2.5$ s). Whole brain coverage for the functional data was obtained using 32 contiguous interleaved 4 mm axial slices.

Data pre-processing

Functional images were first processed to reduce artifacts (Miezin et al., 2000). These steps included: (i) removal of a central spike caused by MR signal offset, (ii) correction of odd versus even slice intensity differences attributable to interleaved acquisition without gaps, (iii) correction for head movement within and across runs and (iv) within run intensity normalization to a whole brain mode value of 1000. Atlas transformation of the functional data was computed for each individual using the MP-RAGE scan. Each run was then resampled in atlas space on an isotropic 3 mm grid combining movement correction and atlas transformation in a single interpolation (Lancaster et al., 1995; Snyder, 1996).

rs-fcMRI pre-processing

For rs-fcMRI analyses, several additional preprocessing steps were utilized to reduce spurious variance unlikely to reflect neuronal activity (Fox et al., 2009). These steps included: (i) a temporal band-pass filter ($0.009 \text{ Hz} < f < 0.08 \text{ Hz}$) and spatial smoothing (6 mm full width at half maximum), (ii) regression of six parameters obtained by rigid body head motion correction, (iii) regression of the whole brain signal averaged across the whole brain, (iv) regression of ventricular signal averaged from ventricular regions of interest (ROIs), and (v) regression of white matter signal averaged from white matter ROIs. The first derivatives of these regressors were also regressed.

Meta-analytic ROI definition

The first method of identifying putative functional areas searched a large fMRI dataset (dataset 1) for brain regions that reliably displayed significant activity when certain tasks were performed (e.g. button-pressing) or certain signal types (e.g. error-related activity) were expected. Studies performed within our laboratory were gathered, and a series of meta-analyses, focused on error processing, task-induced deactivations, memory, language and sensorimotor functions were carried out to identify putative functional areas (Table S1). Some subject overlap occurred between meta-analyses. For the sensorimotor and language meta-analyses, main effect of activation (ANOVA: time as single factor over 7 levels) statistical images were generated from each included study. To identify voxels that were reliably activated across these studies, the activation images were thresholded at a high Z-score ($Z > 7$). The error (2-factor ANOVA: correctness (2-levels) x time (7-levels)) and memory-related (2-factor ANOVA: oldness (2-levels) x time (7-levels)) meta-analyses relied on statistically weaker interaction effects, and thresholds were scaled appropriately lower (error: $Z > 4$; memory: $Z > 2$). The task-induced deactivation regions were derived from meta-analyses of both trial-related ($Z > 7$; main effect of deactivation) and sustained deactivations ($Z > 2$). As in the analysis of interactions, a lower threshold was applied to the sustained signals since they are less reliable statistically. Several thresholds on statistical maps were tested initially, and the peaks identified were very similar. Additionally, there was substantial overlap in identified peaks between meta-analyses, and so small differences in peaks identified from a single meta-analysis were offset by redundancies with other meta-analyses.

For each study in a meta-analysis, voxels passing the threshold were set equal to one and all others equal to zero, creating a mask of significantly activated voxels for each study. The masks for all studies were summed to create a conjunction image, where each voxel carried a value between zero and the number of studies in the meta-analysis, indicating how often voxels were significantly activated across the meta-analysis. After applying a 4 mm smoothing kernel to these images, peak-finding algorithms were used to identify centers of reliably activated groups of voxels. This identified 322 ROIs across the cortex, subcortical structures, and cerebellum, shown in Figure S1.

Several steps were taken to reduce the 322 ROIs to a collection of non-overlapping ROIs.

(i) 10 mm diameter spheres were centered at the activity peaks for each meta-analysis to identify overlapping ROIs. (ii) ROIs from the error processing and task-induced deactivation meta-analyses were given preference. (iii) Overlapping ROIs from the remaining language, memory and sensorimotor meta-analyses were spatially averaged

to produce non-overlapping ROIs. (iv) The consolidated language, memory, and sensorimotor ROIs were added to the ROIs of (ii) if they did not overlap. Previously published cognitive control regions were included in the set of error-processing related regions (Dosenbach et al., 2006). In this manner, a total of 165 ROIs were generated, from which 14 were pruned for sitting too close to white matter or the tentorium. This generated a final set of 151 meta-analytic ROIs. Results from a subset of these 165 ROIs have been previously reported (Dosenbach et al., 2010).

fc-Mapping ROI definition

fc-Mapping techniques were applied to eyes-open fixation rs-fcMRI data from 40 healthy young adults (dataset 2: 27M/13F, average age = 26.4 years old, average RMS movement = 0.42 mm, average number of volumes = 432). Interested readers are referred to (Cohen et al., 2008) and (Nelson et al., 2010) for full conceptual and technical descriptions of fc-Mapping on cortical patches. Here, patches extending over the entire cortical surface (one per hemisphere) were used to define putative functional areas.

This technique generated 254 ROIs across the cortex, ~~many of which were within 10 mm of one another~~. To obtain a non-overlapping set of ROIs for analysis, encroaching ROIs were randomly eliminated until no overlapping ROIs remained. This random elimination process can generate many slightly different collections of ROIs. Here, a typical collection of 193 is used. Many collections were tested, and all variants had very similar network structures. ROIs near the tentorium were removed by visual inspection.

Areal ROI set formation

Meta-analytic ROIs and fc-Mapping ROIs were merged to form a maximally-spanning collection of ROIs. Meta-analytic ROIs were given preference, and non-overlapping fc-Mapping ROIs were then added to form the combined ROI set, **resulting in 264 combined ROIs**, whose coordinates are listed in Table S2.

Parcel-based and voxel-based network formation

A 90-node parcel-based network was formed by using the 90-parcel Automated Anatomical Labeling (AAL) atlas (Tzourio-Mazoyer et al., 2002) to assign all voxels (N=44,100) within the atlas into 90 parcels. An average timecourse was formed for each parcel by averaging the timecourses of all nodes within the parcel. A 44,100-node voxelwise network was defined from all voxels within the Automated Anatomical Labeling (AAL) atlas (Tzourio-Mazoyer et al., 2002). The modified voxelwise networks arose by masking out edges that terminated within 20 mm of the source voxel. Distances of 15-25 mm were tested, with similar results across networks. Analyses were performed on all voxels in both hemispheres (N = 44,100), and also on all voxels within a single hemisphere (N = 22,050). Single hemisphere analyses were much less computationally demanding, permitting a wider range of analysis, and results between single- and dual-hemisphere analyses were similar. Except for Figure 3, all figures use single-hemisphere results.

Formation of two subject cohorts for rs-fcMRI network analysis

rs-fcMRI networks were studied in continuous eyes-open fixation data from two cohorts (dataset 3) of healthy young adults, matched for age, sex, movement and number of

volumes in scans, as shown in Table S1. These subjects underwent a rigorous quality control process to minimize effects of head motion (Power et al., 2011). Data quality was insured using 2 independent checks. The first check used realignment parameters to index subject movement and identify frames that might be of poor quality. For each subject, the BOLD runs that were used in functional connectivity analysis were identified, and realignment parameters were used to index subject movement. A framewise displacement of the brain was calculated (the sum of the absolute values of the differentials of the 3 translational parameters and the 3 rotational parameters calculated at a distance of 50 mm), and frames whose displacement from the previous frame exceeded 0.5 mm were flagged. The second check used the functional connectivity image itself, rather than realignment parameters. Here, a temporal derivative was calculated on the BOLD signal at every voxel, and at each frame, an index was formed from the root mean square (RMS) of these voxelwise timecourse derivatives. Frames where this index exceeded 0.5% Δ BOLD were flagged, identifying frames where BOLD signal across the entire brain (or substantial portions of it) was changing rapidly. For functional connectivity analysis, all flagged frames were ignored, as well as frames 2 forward and 1 back from any flagged frame, to produce the final functional image from which timeseries were extracted. Reported numbers of volumes and RMS are for the final, usable, data (Table S1). Data cleaning removed 6% of the data from subjects (range 4-8%), and each cohort contained a mean of 350 frames of data per subject (range 215-501 frames). The single subject in Figure 2 had 1181 frames of data.

rs-fcMRI graph formation

Given a collection of N ROIs (parcels, voxels, or putative areas), within each subject, timecourses are extracted for all ROIs and an $N \times N$ correlation matrix is calculated. An average matrix is formed across all subjects in a cohort, and the diagonal is set to zero. This defines a weighted graph.

Typical graph analyses of weighted networks ignore negative edges and are obliged to explore a range of thresholds to characterize the properties of a network (Power et al., 2010; Rubinov and Sporns, 2009). Recent proposals to incorporate negative weights into analyses of community detection have been made (Gómez et al., 2009; Kaplan and Forrest, 2008; Traag and Bruggeman, 2009; Rubinov and Sporns, 2011), but here we follow the traditional approach. Many real-world networks have edge densities of a few percent (Newman, 2010), and the graph analytic techniques utilized here were developed upon such networks (Fortunato, 2010; Newman, 2010; Rosvall and Bergstrom, 2008). Accordingly, the analyses presented here typically span a threshold range on the order of 10% down to 1% edge density though the precise range depends upon the network (for example, the AAL-based parcel network is severely fragmented at 4% edge density and we do not present results from this threshold). In general, results are presented over a range of thresholds (in Figures and Supplemental Materials) to give the reader a sense of the dependence of a property upon thresholds, and no formal definition of threshold ranges is proposed, since it is essentially arbitrary.

As noted in the text, short-range correlations can arise from shared patterns of local neuronal activity, but they can also arise from aspects of data processing (e.g. reslicing, blurring), as well as motion-induced artifacts (Power et al., 2011). Local correlations are

thus combinations of neurobiological and artifactual signal. To minimize the effects of questionable correlations on network structure, edges terminating within 20 mm of the source ROI are set to zero in all areal network analyses and in the modified voxelwise analysis. Although this does not completely remove the effect of reslicing and blurring on correlations in the data (consider a voxel's correlations to distant but adjacent voxels), it removes a considerable portion of correlations of questionable origin. This procedure eliminated 635 (4.1%) of the 15,375 positive edges in the combined network, and 15.3 million (4.2%) of 470 million edges in the single hemisphere voxelwise network.

Community Detection and Graph Analysis

For a given network at a given threshold, the correlations below the threshold were set to zero, and the resulting matrix was subjected to a community detection algorithms. Many community detection algorithms are available, each with strengths and weaknesses. We utilized the Infomap algorithm, which uses the Map Equation (Rosvall and Bergstrom, 2008) to minimize an information theoretic description of a random walker over the network to define communities (Rosvall and Bergstrom, 2008). This algorithm is among the best-performing algorithms on multiple benchmark networks (Fortunato, 2010; Lancichinetti and Fortunato, 2009). Other algorithms were tried, which returned similar results (Figure S2). Community assignments were returned as numbers, which were then mapped onto nodes and ROIs as colors. For areal networks, nodes are plotted as colored foci on PALS inflated surfaces (Van Essen, 2005). For parcel- and voxel-based networks, nodes are plotted as colored PALS surfaces and as 2-D sections of a brain volume (see relevant Supplemental Materials).

Local efficiency was calculated after (Latora and Marchiori, 2001). Participation coefficients were calculated after (Guimerà et al., 2005). Binary networks were used for calculations.

Computations and Visualizations

MRI images were processed using in-house software. Network calculations were performed using MATLAB (2007a, The Mathworks, Natick, MA). The Infomap algorithm was provided by Rosvall et al. (Rosvall and Bergstrom, 2008). Network visualizations were created using the Social Network Image Animator (SoNIA) software package (Bender-deMoll and McFarland, 2006). For spring embedding plots, nodes were randomly placed in a 2D plane, springs with attractive forces related to edge weights were placed between nodes, and the nodes were iteratively moved to relax the spring system according to the Kamada-Kawai algorithm to produce a layout of the network in a "natural" or "low-energy" state. Brain surface visualizations were created using Caret software and the PALS surface (Van Essen, 2005; Van Essen et al., 2001).

Supplemental References:

Gómez, S., Jensen, P., and Arenas, A. (2009). Analysis of community structure in networks of correlated data. *Physical Review. E, Statistical, Nonlinear, and Soft Matter Physics* 80, 016114.

Kaplan, T.D., and Forrest, S. (2008). A dual assortative measure of community structure %U <http://arxiv.org/abs/0801.3290>. 0801.3290.

Lancaster, J.L., Glass, T.G., Lankipalli, B.R., Downs, H., Mayberg, H., and Fox, P.T. (1995). A Modality-Independent Approach to Spatial Normalization of Tomographic Images of the Human Brain. *Hum Brain Mapp* 3, 209-223.

Miezin, F.M., Maccotta, L., Ollinger, J.M., Petersen, S.E., and Buckner, R.L. (2000). Characterizing the hemodynamic response: Effects of presentation rate, sampling procedure, and the possibility of ordering brain activity based on relative timing. *NeuroImage* 11, 735-759.

Snyder, A.Z. (1996). Difference image vs. ratio image error function forms in PET-PET realignment. In *Quantification of Brain Function Using PET*, R. Myer, V.J. Cunningham, D.L. Bailey, and T. Jones, eds. (San Diego, CA: Academic Press), pp. 131-137.

Traag, V.A., and Bruggeman, J. (2009). Community detection in networks with positive and negative links. *Physical Review. E, Statistical, Nonlinear, and Soft Matter Physics* 80, 036115.